Volume 11 · No. 8 – February 25 2015

NANO MICRO

small

www.small-journal.com

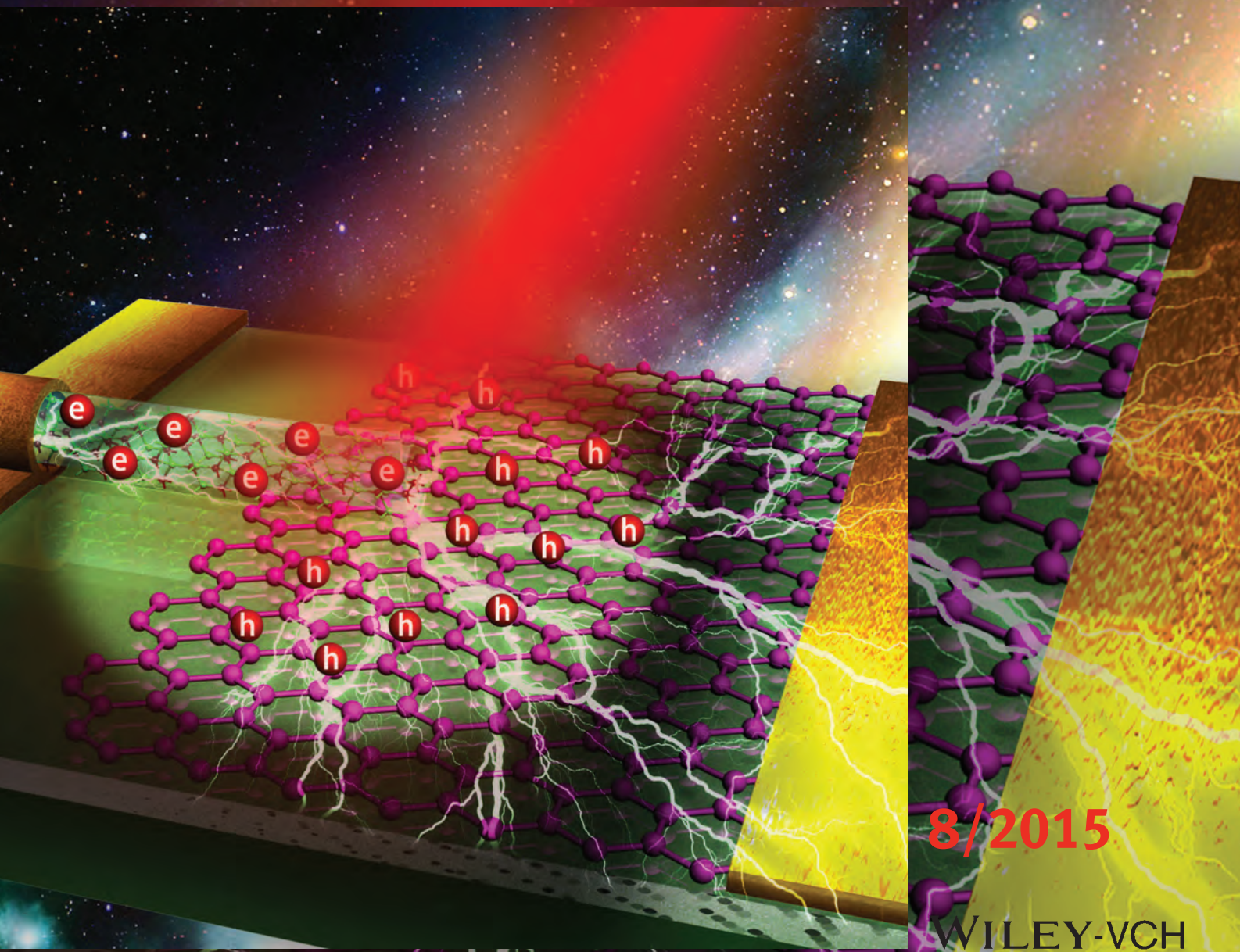

8/2015

WILEY-VCH

High-Responsivity Graphene/InAs Nanowire Heterojunction Near-Infrared Photodetectors with Distinct Photocurrent On/Off Ratios

W. Hu, L. Liao, and co-workers

www.MaterialsViews.com

High-Responsivity Graphene/InAs Nanowire Heterojunction Near-Infrared Photodetectors with Distinct Photocurrent On/Off Ratios

Jinshui Miao, Weida Hu, Nan Guo, Zhenyu Lu, Xingqiang Liu, Lei Liao,* Pingping Chen, Tao Jiang, Shiwei Wu, Johnny C. Ho, Lin Wang, Xiaoshuang Chen, and Wei Lu*

Graphene is a promising candidate material for high-speed and ultra-broadband photodetectors. However, graphene-based photodetectors suffer from low photoreponsivity and I_{light}/I_{dark} ratios due to their negligible-gap nature and small optical absorption. Here, a new type of graphene/InAs nanowire (NW) vertically stacked heterojunction infrared photodetector is reported, with a large photoresponsivity of 0.5 AW^{-1} and I_{light}/I_{dark} ratio of 5×10^2, while the photoresponsivity and I_{light}/I_{dark} ratio of graphene infrared photodetectors are 0.1 mAW^{-1} and 1, respectively. The Fermi level (E_F) of graphene can be widely tuned by the gate voltage owing to its 2D nature. As a result, the back-gated bias can modulate the Schottky barrier (SB) height at the interface between graphene and InAs NWs. Simulations further demonstrate the rectification behavior of graphene/InAs NW heterojunctions and the tunable SB controls charge transport across the vertically stacked heterostructure. The results address key challenges for graphene-based infrared detectors, and are promising for the development of graphene electronic and optoelectronic applications.

1. Introduction

Graphene, a single layer hexagonal lattice of carbon atoms, is emerging as an attractive candidate material for next-generation electronics and optoelectronics since it was isolated in 2004 due to its exceptionally high carrier mobility, unique optical characteristics, and superb

J. Miao, Prof. W. Hu, N. Guo, Z. Lu, Prof. P. Chen, L. Wang, Prof. X. Chen, Prof. W. Lu
National Laboratory for Infrared Physics
Shanghai Institute of Technical Physics
Chinese Academy of Sciences
500 Yutian Road, Shanghai 200083, China
E-mail: wdhu@mail.sitp.ac.cn

X. Liu, Prof. L. Liao
Department of Physics and Key Laboratory of Artificial Micro- and Nano-structures of Ministry of Education
Wuhan University
Wuhan 430072, China
E-mail: liaolei@whu.edu.cn

Prof. J. C. Ho
Department of Physics and Materials Science
City University of Hong Kong, SAR, China

T. Jiang, Prof. S. Wu
State Key Laboratory of Surface Physics and Department of Physics
Fudan University
Shanghai 200433, China

J. Miao, Prof. W. Hu, N. Guo, Z. Lu, Prof. P. Chen, L. Wang, Prof. X. Chen, Prof. W. Lu
Synergetic Innovation Center of Quantum Information and Quantum Physics
University of Science and Technology of China
Hefei, Anhui 230026, China

DOI: 10.1002/smll.201402312

mechanical flexibility.[1–13,48–50] The unusual band structure makes it a negligible-gap semiconductor with a linear energy dispersion relation, indicating a vanishing effective mass, a high Fermi velocity, and a high carrier mobility of 200,000 $cm^2V^{-1}s^{-1}$.[13–17] Despite its single atomic layer, graphene can absorb photons of energy ranging from the visible to the mid-infrared region (400 nm to 6 μm).[18] Therefore, graphene is particularly desirable for high-speed and ultrabroadband photodetectors with its fast carrier transport, wide absorption spectrum, and a short lifetime of photogenerated electron-hole pairs.[18–21] Previous studies of graphene-based photodetectors have indicated that the photocurrent generated near metal/graphene contacts resulted from the internal (built-in) electric field at the interface, which separated the photogenerated electron-hole pairs.[18,20] Graphene p-n junctions could also be achieved through the top-gated bias modulation and chemical doping.[22–27] In this way, the photocurrent generated at these p-n interfaces was attributed to a combination of direct photogenerated electron-hole pairs in a potential gradient and a photothermoelectric effect.[27–29] However, the negligible-gap nature of graphene results in ultralow photoresponsivity (~mA/W) of graphene field-effect transistors (FETs).[21] Importantly, the large dark current of graphene-based photodetectors leads to a very low signal-to-noise ratio (SNR). In this regard, several strategies were proposed to address these challenges including graphene nanoribbons,[4] manipulation of bilayer graphene,[31] barristors,[17] graphene-semiconductor heterostructures,[44–46] and vertically tunneling devices.[30] However, to the best of our knowledge, no room-temperature graphene/semiconductor NW heterojunction near-infrared photodetectors have been reported. With unique one-dimensional (1D) structural characteristics and versatile physical properties, semiconductor NWs have received considerable attention as potential building blocks for various fundamental optical and electronic devices or systems.[32–43] In particularly, InAs NW is a promising candidate material for near-infrared detection due to its narrow band-gap for infrared detection, high carrier mobility, large surface-to-volume ratio, ease of Ohmic contacts, and high photoresponsivity.[32] In this case, with the goal of a high I_{light}/I_{dark} ratio and significant photoresponsivity, it is necessary and easier to introduce heterojunctions into the graphene photodetectors, rather than opening up the energy gap or fabricating p-n junctions in view of the complicated fabrication processes for graphene ribbons, manipulation of gate bias, or chemical doping.[17,22–24]

Here we report on vertically stacked graphene/InAs NW heterojunction near-infrared photodetectors with a distinct I_{light}/I_{dark} ratio of 5×10^2 in the infrared region (λ = 1 μm), which is much larger than that of graphene infrared photodetectors (I_{light}/I_{dark} ratio is ~1). Moreover, the heterojunction detectors have a high photoresponsivity of 0.5 AW^{-1}, which is in contrast with graphene infrared photodetectors (0.1 mAW^{-1}). Additionally, a similar device with a graphene/CdS NW configuration has been fabricated and demonstrated. The graphene/CdS NW heterojunction photodetectors have a high I_{light}/I_{dark} ratio of 10^4 in the visible region (λ = 532 nm), while the I_{light}/I_{dark} ratio of a single CdS NW detector is only 10. The graphene used in this work was mechanically exfoliated from natural graphite flake onto p^+-Si/SiO_2 (300 nm) substrates. Then, InAs (or CdS) NWs were physically transferred onto the substrates, followed by the definition of source/drain (S/D) electrodes on the graphene and NW, respectively, through electron-beam-lithography (EBL), metallization, and lift-off processes. The exfoliated graphene in contact with the source electrode forms heterojunction at the interface connecting with semiconductor NWs at the drain electrode side. The S/D electrodes of graphene/InAs NW heterojunction photodetectors were Cr/Au (20 nm/40 nm), while the graphene/CdS NW heterojunction photodetectors employed metal Ti/Au (20 nm/40 nm) as S/D electrodes.

2. Results and Discussions

To investigate the photocurrent response of graphene infrared photodetectors, a scanning photocurrent microscopy (SPM) was used in this work. A beam of monochromatic laser light (λ = 532 nm) is focused with an objective lens onto the detectors resulting in a spot of ~1 μm in diameter. **Figure 1**a displays the optical microscope image of a typical graphene FETs which shows the channel length of L ~ 20 μm and channel width of W ~ 8 μm. For the detection of photocurrent, the laser beam is modulated at the frequency of f ~ 859 Hz with a mechanical chopper. Figure 1b presents the spatially resolved photocurrent mapping obtained by scanning the focused laser spot over the device while measuring the output current via a lock-in amplifier. It is found that a strong photocurrent is generated at the metal/graphene interfaces (Points A and C) which is attributed to the separation of photogenerated electron-hole pairs by internal (built-in) electric fields. The internal electric fields could form at these interfaces because of a potential difference established between the graphene covered by metal electrodes and the uncovered part.[31] On the other hand,

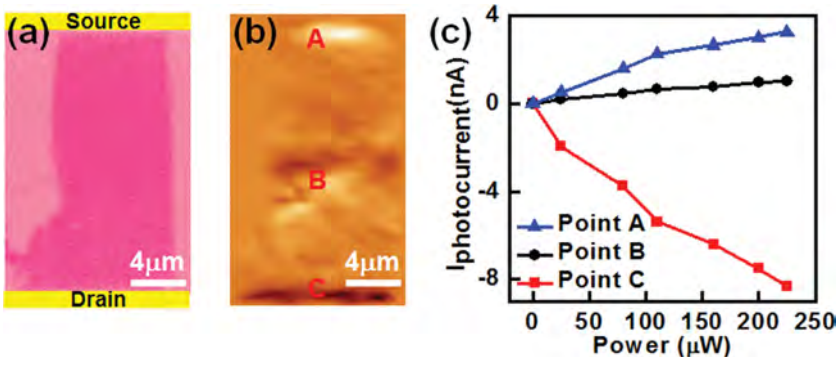

Figure 1. (a) Optical microscope image of back-gated graphene FETs. (b) Spatially resolved photocurrent mapping at room temperature with the laser wavelength of λ = 532 nm and optical power of 150 μW. (c) I_{photo} as a function of the incident power taken at point A, B, and C from Figure 1b and the laser wavelength is 1 μm.

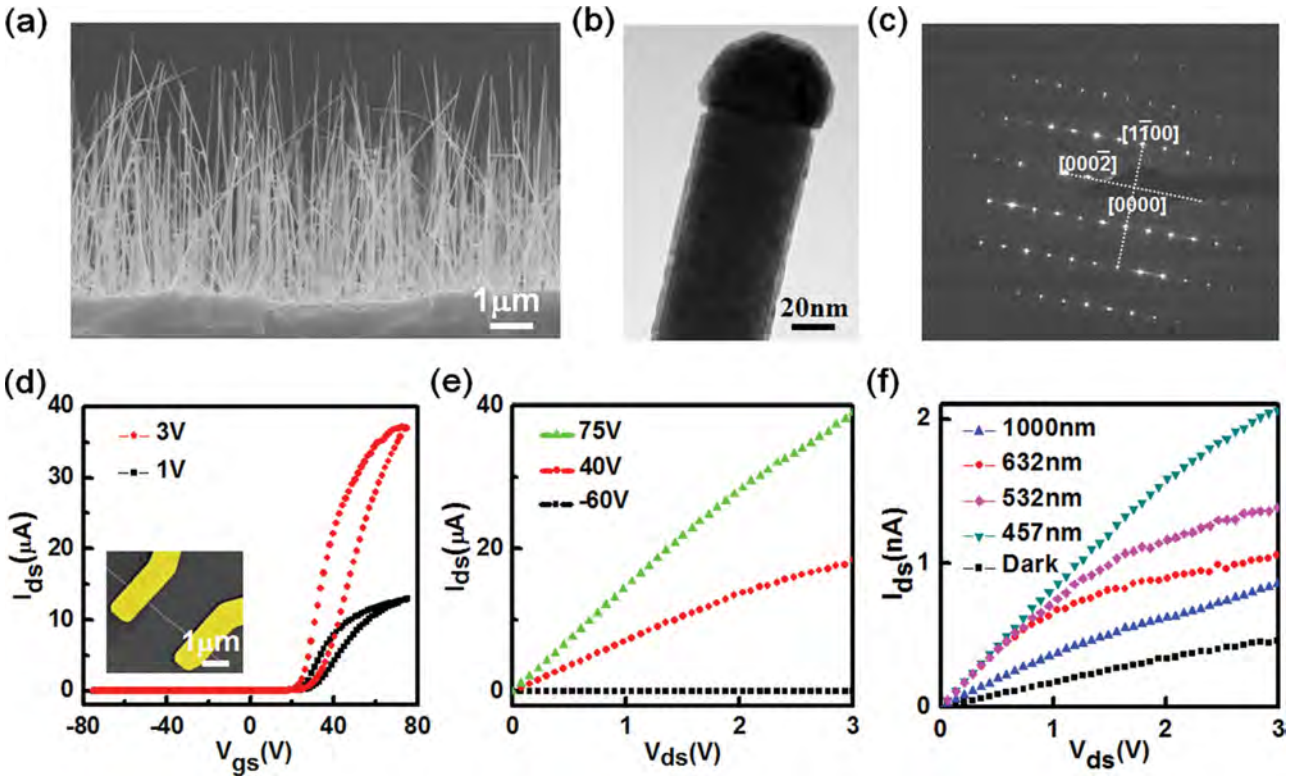

Figure 2. (a) SEM image of InAs NWs. (b) TEM image of a representative single InAs NW and (c) corresponding selected area of electron diffraction (SAED) pattern. (d) I_{ds} versus V_{gs} transfer characteristics of InAs NW FETs. Inset is the SEM image of an InAs NW FET. (e) I_{ds} versus V_{ds} output characteristics of the same device. (f) Photocurrent spectrum of InAs NW infrared photodetectors ranging from blue (457 nm) to near-infrared (1 μm) light.

the photocurrent at point B is weak due to the absence of a strong built-in field in the bulk graphene there. Therefore, most photogenerated electron-hole pairs would recombine before flowing into the S/D electrodes, without any contribution to the photocurrent. Figure 1c illustrates the infrared photocurrent as a function of illuminated laser power ($\lambda = 1$ μm) with the laser spot located at point A, B, and C. The infrared photocurrent at point A and B has different polarities corresponding to the spatially resolved photocurrent map indicated in Figure 1b. This is because the internal electric fields at point A and B have opposite directions resulting in the separation of photogenerated electron-hole pairs in opposite ways. As a result, the maximum photoresponsivity is ~0.1 mA/W, as shown in Figure 1c. The photo-induced transfer ($I_{ds} \sim V_{gs}$) and output ($I_{ds} \sim V_{ds}$) characteristics of the same graphene FETs (Figure S1, Supporting Information) show that the average I_{light}/I_{dark} ratio is ~1, which is mainly due to the negligible gap in graphene.

The InAs NWs were synthesized on GaAs $(111)_B$ substrates by molecule beam epitaxy (MBE) technique. **Figure 2**a presents the SEM image of InAs NWs indicating that the NWs have an average length of ~6 μm and diameter of ~50 nm. The typical high-resolution transmission electron microscopy (HRTEM) image is presented in Figure 2b. It shows that the InAs NW appears relatively homogeneous without any obvious domain boundaries, illustrating its single-crystalline nature. It also shows that the InAs NW has a native oxide layer ($L \sim 2$ nm). Figure 2c presents the corresponding selected area of electron diffraction (SAED) pattern, which shows that the InAs NW has a wurtzite single-crystal structure with a dominate growth direction of [0001]. To shed light on the electrical performance of InAs NWs, FETs were fabricated by using metal Cr/Au (20 nm/40 nm) as S/D electrodes on a p^+-Si/SiO_2 (300 nm) substrate. The representative FETs consist of a single InAs NW as the channel material with length of $L \sim 2$ μm and diameter of $d \sim 50$ nm, as shown in the SEM image of Figure 2d (inset). The device displays a minimum hysteresis with on-current $I_{on} \sim 30$ μA in the vacuum condition. Moreover, the device has a very high I_{on}/I_{off} ratio of 5×10^4. Figure 2e shows the drain current *versus* drain voltage ($I_{ds} \sim V_{ds}$) output characteristics of the same FETs at various back-gated biases. The linear behavior of output characteristics demonstrates the good Ohmic contacts. Figure 2f presents the photocurrent spectrum of InAs NW infrared photodetectors ranging from blue (457 nm) to near-infrared (1 μm) light. It is found out that the detectors have distinct photocurrent response under illumination. Figure S2 (Supporting Information) shows the *I*–*V* characteristics of InAs NW array FETs. The device has a maximum on-current $I_{on} \sim 0.1$ mA and I_{on}/I_{off} ratio of 10^4. InAs NWs are sensitive to chemical molecules, due to their large surface-to-volume ratio, existence of an intrinsic electron accumulation layer, and rich surface defect states. Figure S3 (Supporting Information) presents the $I_{ds} \sim V_{gs}$ transfer characteristics of InAs NW FETs in the ambient atmosphere or vacuum condition. The device hysteresis decreased when it was in the vacuum condition and the on-current decreased slightly after introducing the

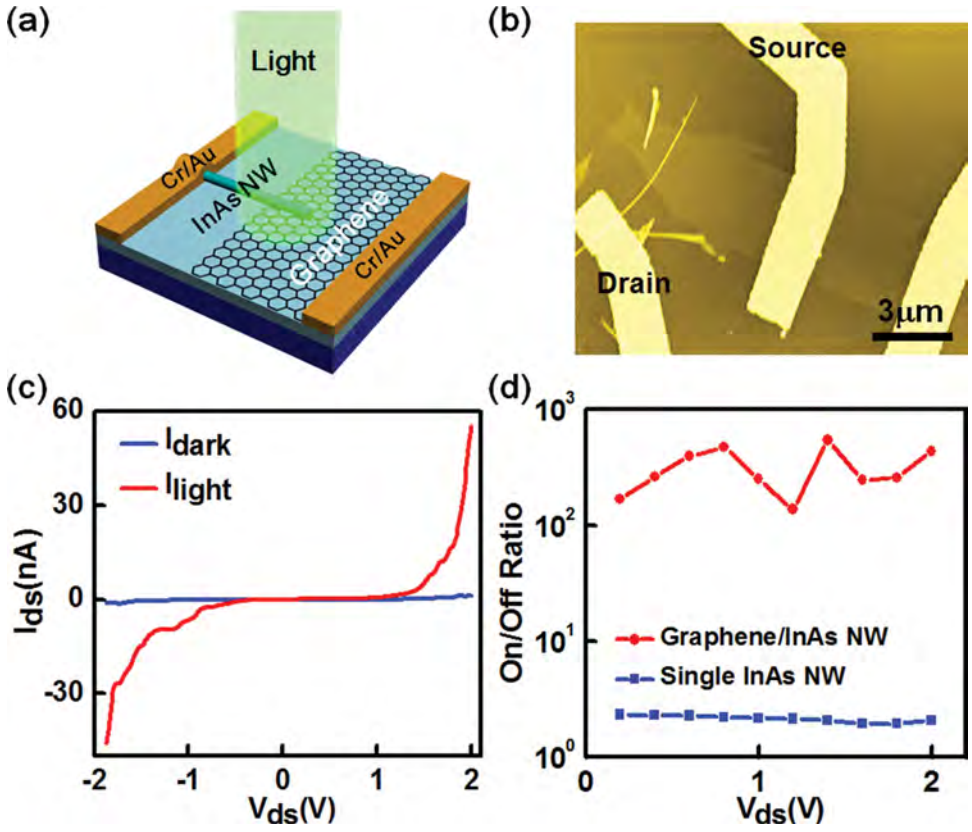

Figure 3. (a) Schematic of graphene/InAs NW heterojunction near-infrared photodetectors. (b) SEM image of graphene/InAs NW heterojunction device. (c) Photo-induced I_{ds} versus V_{ds} output characteristics of graphene/InAs NW heterojunction device. (d) Comparison of I_{light}/I_{dark} ratios of graphene/InAs NW heterojunction infrared photodetectors and single InAs NW infrared photodetectors. The incident laser wavelength is 1 μm.

ambient atmosphere. This is mainly attributed to electron transfer from InAs NWs to the adsorbed atmospheric molecules. As a result, the carrier density decreased. Moreover, the carrier mobility also decreased owing to scattering between surface carriers and adsorbed atmospheric molecules. Figure S4 (Supporting Information) shows the *I–V* characteristics of top-gated InAs NW FETs in the atmosphere condition. The InAs NWs were passivated with 10 nm HfO_2 dielectric via atomic layer deposition (ALD). The HfO_2 passivation layer not only reduces the surface defect states of InAs NWs, but also suppresses the negative effects of atmospheric molecules. Thus it can improve the electrical performance of InAs NW photodetectors.

The graphene/InAs NW heterojunction near-infrared photodetectors have been successfully fabricated in the experiment, as presented in the schematic of **Figure 3**a. It is difficult to form graphene/InAs NW heterojunction contacts, since the InAs NWs have a native oxide layer, as shown in Figure 2b. To resolve the problem, the InAs NWs were dipped into 2% HF solution for 15 s to remove the native oxide before being transferred onto graphene. Based on the SEM image (Figure 3b) it is found out that about half of the InAs NW is in contact with the exfoliated graphene. Figure 3c gives the output characteristics ($I_{ds} \sim V_{ds}$) of a representative graphene/InAs NW heterojunction near-infrared photodetectors under the dark and illumination condition. And the incident laser wavelength is 1 μm. The photodetector has a large I_{light}/I_{dark} ratio of ~5×10^2 and photoresponsivity of ~0.5 AW^{-1}. The photoresponsivity can be calculated by the following equation:[33]

$$R = \frac{I_{ph}}{P \cdot S} \quad (1)$$

where the I_{ph} is the photocurrent of the detectors, P is the power density of the incident light (~1 Wcm^{-2}), and S is the effective illuminated area of 10 μm^2. Figure 3d shows the comparison of I_{light}/I_{dark} ratios of the graphene/InAs NW heterojunction near-infrared photodetectors and single InAs NW near-infrared photodetectors. The maximum I_{light}/I_{dark} ratio of single InAs NW infrared photodetectors is less than 5 which is much smaller than that of the graphene/InAs NW infrared photodetectors (~5×10^2). Therefore, the existence of graphene/InAs NW heterojunctions improves the I_{light}/I_{dark} ratio of the infrared detectors.

To better understand the mechanism of graphene/InAs NW heterojunction near-infrared photodetectors, schematic energy band diagram was introduced, as depicted in **Figure 4**a. The typical workfunction (W) of graphene and intrinsically n-type InAs NW is ~4.5 eV and ~5.0 eV, respectively.[14,51–53] Since the E_F of graphene can be adjusted over a wide range by the top/bottom voltage due to its 2D nature.[7,14] Therefore the workfunction of graphene (W_{gra}) in devices can be different with changing top/bottom voltages. A heterojunction could form at the interface between the InAs NW and graphene because of the different workfunction and band energy. Typically, due to W_{gra} (4.5 eV) < W_{InAs} (5.0 eV),

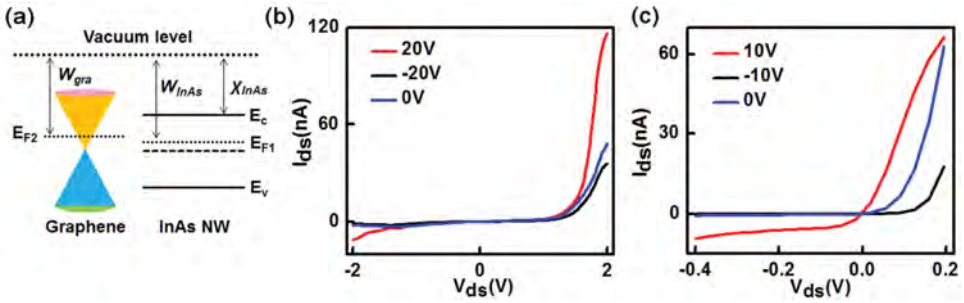

Figure 4. (a) Schematic energy band diagram of graphene/InAs NW heterostructure. (b) Experiment result of I_{ds} versus V_{ds} output characteristics of graphene/InAs NW heterojunction device. (c) Simulation result of I_{ds} versus V_{ds} output characteristics of graphene/InAs NW heterojunction device.

this is Ohmic contact, and no SB exists at all. Changing the device bottom-gate voltage leads to $W_{gra} > W_{InAs}$, and the SB height (ϕ_B) can be expressed as $\phi_B = W_{gra} - \chi_{InAs}$ (fixed, electron affinity) and this is the blocking contact.[47,51–53] When a positive V_{gs} is applied:

$$+V_{gs} \Rightarrow n_e \uparrow \Rightarrow E_F \uparrow \Rightarrow W_{gra} \downarrow \quad (2)$$

The positive back-gated voltage can reduce the graphene/InAs NW SB height, allowing electrons to readily overcome the SB height through thermionic emission process. As a result, the current becomes larger as the back-gated voltage is increased. Figure 4b shows the experiment result of I_{ds} versus V_{ds} output characteristics of graphene/InAs NW heterojunction photodetectors. It is found out that the output current is much higher at positive V_{ds}. Moreover, the current becomes smaller and smaller as the back-gated voltage changes from 20 V to –20 V (from red line to black line). The diode-like I_{ds} versus V_{ds} curves in Figure 4b demonstrates the existence of heterostructures in the as fabricated detectors. Figure 4c shows the simulation result of I_{ds} versus V_{ds} output characteristics of graphene/InAs NW heterojunction photodetectors. The details of simulation method for graphene FETs can be found in the literature.[48] (from equation 3 to 7). The simulation result perfectly matches with the experiment result. Since the existed heterostructures can reduce the dark current of graphene/InAs NW heterojunction photodetectors, the devices have a large photocurrent on/off ratio under illumination, as shown in Figure 3c.

Additionally, a similar photodetector with a graphene/CdS NW configuration has also been fabricated and demonstrated, as shown in **Figure 5**. Figure 5a shows the SEM image of CdS NWs, indicating that the NWs are uniform with the length of ~20 μm and diameter of ~50 nm. The photoluminescence (PL) spectrum of CdS NWs presents a relatively narrow peak around 500 nm (Figure 5b). Figure 5c displays the SEM image of a representative graphene/CdS NW heterojunction photodetector. The photodetector was fabricated by employing Ti/Au (20 nm/40 nm) as S/D electrodes on a p^+-Si/SiO_2 (300 nm) substrate. Figure 5d shows the photo-induced output characteristics ($I_{ds} \sim V_{ds}$) of a graphene/CdS NW heterojunction photodetectors and the incident wavelength is 532 nm. The photodetector presents a high I_{light}/I_{dark} ratio of 10^4. To expand, Figure 5e displays the fast I_{light}/I_{dark}

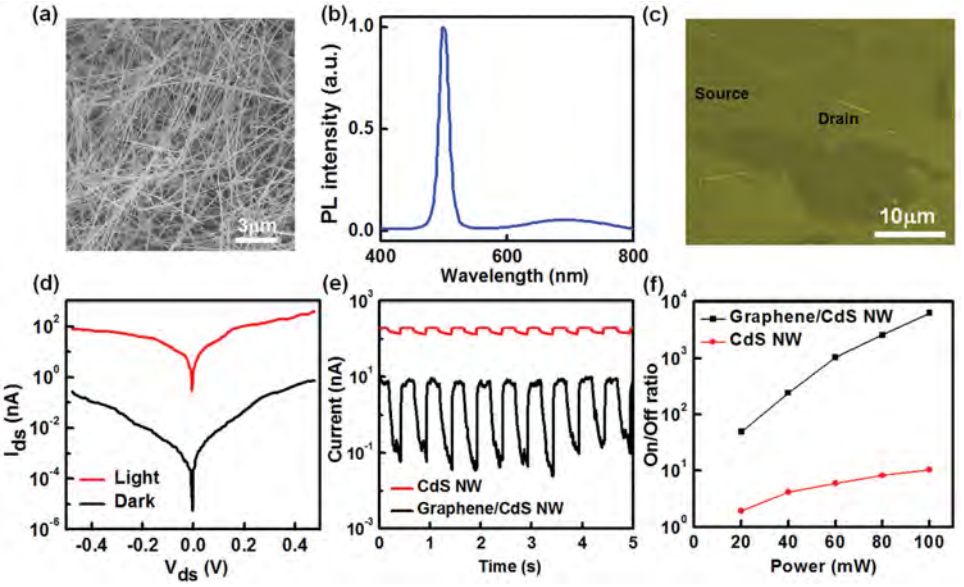

Figure 5. (a) SEM image of CdS NWs. (b) Photoluminescence (PL) spectrum of CdS NWs. (c) SEM image of a representative graphene/CdS NW heterojunction photodetector. (d) Photo-induced I_{ds} *versus* V_{ds} logarithmic output characteristics. (e) Time-resolved photoresponse of the same detector. (f) I_{light}/I_{dark} ratio as a function of illumination power. The laser wavelength is 532 nm.

switching behavior of the graphene/CdS NW heterojunction photodetectors and single CdS NW photodetectors with different chopping frequencies. Notably, the single CdS NW photodetectors exhibit an insignificant I_{light}/I_{dark} ratio. However, the I_{light}/I_{dark} switching behavior of the graphene/CdS NW heterojunction photodetectors is still well maintained even when the chopping frequency is 250 Hz (Figure S5, Supporting Information). These effects indicate that the large I_{light}/I_{dark} ratio is mainly attributed to the heterojunction at the graphene and CdS NW interface. Figure 5f shows the I_{light}/I_{dark} ratio as a function of the illumination power indicating that they gradually increased when the incident power increased from 20 mW to 100 mW. The enhanced I_{light}/I_{dark} ratio is mainly attributed to increased number of photogenerated electron-hole pairs as the incident power increases. In this manner, increased incident photon energy would excite electrons from the valence band to conduction band. However, further increase in the illumination power results in photocurrent saturation owning to the heat effect.

3. Conclusions

We have fabricated and investigated graphene/semiconductor NW heterojunction photodetectors. The graphene/InAs NW heterojunction near-infrared photodetectors have a maximum I_{light}/I_{dark} ratio of 5×10^2, which is 10^2 times larger than that of single InAs NW infrared photodetectors (<5). Moreover, the photoresponsivity of graphene/InAs NW heterojunction near-infrared photodetectors (0.5 AW^{-1}) is 5×10^3 times higher than that of graphene near-infrared photodetectors (0.1 mAW^{-1}). Additionally, a similar photodetector with graphene/CdS NW heterojunction configuration displayed a large I_{light}/I_{dark} ratio of 10^4. The output characteristics ($I_{ds} \sim V_{ds}$) of graphene/InAs NW heterojunction detectors taken under different gate biases show that the SB height can be modulated by back-gated voltages and the tunable SB controls charge transport across the vertically stacked structure. Moreover, the simulation method further demonstrates the rectification behavior of graphene/semiconductor NW heterojunction. The results address key challenges for graphene near-infrared photodetectors, and are promising for the development of graphene-based electronics, optoelectronics, photonics, and their integrated systems applications.

4. Experimental Section

Growth of InAs NWs: The InAs NWs were synthesized on GaAs $(111)_B$ substrates in a Riber 32 MBE system by the vapor-liquid-solid (VLS) growth mechanism. The GaAs substrate surface was deoxidized at 630 °C for 15 minutes, and then a 300 nm thick GaAs buffer layer was grown in order to obtain a smooth surface. An ultrathin Au film was deposited on GaAs substrates from the Knudsen cell in the MBE preparation chamber followed by the transfer to the growth chamber and annealing at 550 °C for 5 minutes in the As_4 ambient to obtain gold particles. InAs NWs were grown at 350 °C after switching the indium source. The ratio of indium/As_4 was 1:20 and the growth time was 90 minutes. After the growth, the substrates were cooled down to 300 °C with the As_4 overpressure. Finally, the substrates were cooled down to the room temperature naturally.

Growth of CdS NWs: The CdS NWs used in this study were synthesized on SiO_2/Si substrates with a chemical vapor deposition (CVD) method based on the vapor-liquid-solid (VLS) mechanism. The SiO_2/Si substrates were pre-coated with Au particles with 1 nm in thickness, and CdS powder served as the source precursor. The growth of CdS NWs was carried out in a single zone horizontal tube furnace where Ar gas (99.99%) served as both the carrier gas and protective gas. After purging for 20 minutes, the furnace was heated to 850 °C for 30 minutes with an Ar gas flow rate of 200 sccm. Then, the furnace was cooled to room temperature naturally.

Photodetectors Fabrication and Measurements: The graphene used in this work was mechanically exfoliated on p^+-Si/SiO_2 (300 nm) substrates from a graphite flake. Then, CdS or InAs NWs were physically transferred onto the substrates. An optical microscope was used to examine NWs that were in contact with graphene. The EBL (JEOL6510 with NPGS) technique was used to define the S/D patterns. Before metallization, the InAs NWs were dipped into 2% HF solution for 15 s to corrode the native oxide. The Cr/Au (20 nm/40 nm) film was deposited on the NWs to produce S/D electrodes. The NW was in contact with source electrode while the graphene was in contact with drain electrode. The electrical measurements of graphene/semiconductor NW Schottky photodetectors were performed with an Agilent 4155C semiconductor parameter analyzer and Lake Shore TTPX Probe Station.

Supporting Information

Supporting Information is available from the Wiley Online Library or from the author.

Acknowledgements

The authors declare no competing financial interest. This work was supported in part by the State Key Program for Basic Research of China (2014CB921600 and 2011CB932700), and National Natural Science Foundation of China (11322441, 11274331, 11334008, and 61376015), Fund of Shanghai Science and Technology Foundation (14JC1406400), and the Shanghai Rising-Star Program. These acknowledgements were updated on February 25, 2015.

[1] L. Liao, Y. C. Lin, M. Q. Bao, R. Cheng, J. W. Bai, Y. Liu, Y. Q. Qu, K. L. Wang, Y. Huang, X. F. Duan, *Nature* **2010**, *467*, 305.
[2] H. Xu, Y. B. Chen, J. Zhang, H. L. Zhang, *Small* **2012**, *8*, 2833.
[3] L. Liao, J. W. Bai, Y. Q. Qu, Y. C. Lin, Y. J. Li, Y. Huang, X. F. Duan, *Proc. Natl. Acad. Sci. USA* **2010**, *107*, 6711.
[4] Z. Yan, J. Yao, Z. Z. Sun, Y. Zhu, J. M. Tour, *Small* **2012**, *8*, 59.
[5] L. Liao, J. W. Bai, R. Cheng, Y. C. Lin, S. Jiang, Y. Q. Qu, Y. Huang, X. F. Duan, *Nano Lett.* **2010**, *10*, 3952.
[6] L. Liao, J. W. Bai, Y. C. Lin, Y. Q. Qu, Y. Huang, X. F. Duan, *Adv. Mater.* **2010**, *22*, 1941.

[7] Y. Zhang, T. T. Tang, C. Girit, Z. Hao, M. C. Martin, A. Zettl, M. F. Crommie, Y. R. Shen, F. Wang, *Nature* **2009**, *459*, 820.
[8] L. Liao, J. W. Bai, R. Cheng, Y. C. Lin, S. Jiang, Y. Huang, X. F. Duan, *Nano lett.* **2010**, *10*, 1917.
[9] S. W. Wu, W. T. Liu, X. G. Liang, P. J. Schuck, F. Wang, Y. R. Shen, M. Salmeron, *Nano Lett.* **2012**, *12*, 5495.
[10] Y. Liu, R. Cheng, L. Liao, H. L. Zhou, J. W. Bai, G. Liu, L. X. Liu, Y. Huang, X. F. Duan, *Nat. Commun.* **2011**, *2*, 579.
[11] F. Bonaccorso, Z. Sun, T. Hasan, A. C. Ferrari, *Nat. Photonics.* **2010**, *4*, 611.
[12] N. K. Emani, T. F. Chung, X. J. Ni, A. V. Kildishev, Y. P. Chen, A. Boltasseva, *Nano Lett.* **2012**, *12*, 5202.
[13] K. S. Novoselov, A. K. Geim, S. V. Morozov, D. Jiang, Y. Zhang, S. V. Dubonos, I. V. Grigorieva, A. A. Firsov, *Science* **2004**, *306*, 666.
[14] K. S. Novoselov, A. K. Geim, S. V. Morozov, D. Jiang, M. I. Katsnelson, I. V. Grigorieva, S. V. Dubonos, A. A. Firsov, *Nature* **2005**, *438*, 197.
[15] Y. B. Zhang, Y. W. Tan, H. L. Stormer, P. Kim, *Nature* **2005**, *438*, 201.
[16] J. B. Oostinga, H. B. Heersche, X. Liu, A. F. Morpurgo, L. M. Vandersypen, *Nat. Mater.* **2008**, *7*, 151.
[17] H. Yang, J. Heo, S. Park, H. J. Song, D. H. Seo, K. E. Byun, P. Kim, I. Yoo, H. J. Chung, K. Kim, *Science* **2012**, *336*, 1140.
[18] T. Mueller, F. N. Xia, P. Avouris, *Nat. Photonics.* **2010**, *4*, 297.
[19] D. Sun, G. Aivazian, A. M. Jones, J. S. Ross, W. Yao, D. Cobden, X. D. Xu, *Nat. Nanotechnol.* **2012**, *7*, 114.
[20] A. Urich, K. Unterrainer, T. Mueller, *Nano Lett.* **2011**, *11*, 2804.
[21] F. N. Xia, T. Mueller, Y. M. Lin, A. V. Garcia, P. Avouris, *Nat. Nanotechnol.* **2009**, *4*, 839.
[22] W. J. Yu, L. Liao, S. H. Chae, Y. H. Lee, X. F. Duan, *Nano Lett.* **2011**, *11*, 4759.
[23] E. C. Peters, E. J. H. Lee, M. Burghard, K. Kern, *Appl. Phys. Lett.* **2010**, *97*, 193102.
[24] J. R. Williams, L. DiCarlo, C. M. Marcus, *Science* **2007**, *317*, 638.
[25] V. V. Cheianov, V. Falko, B. L. Altshuler, *Science* **2007**, *315*, 1252.
[26] G. Rao, M. Freitag, H. Y. Chiu, R. S. Sundaram, P. Avouris, *ACS Nano* **2011**, *5*, 5848.
[27] M. C. Lemme, F. H. L. Koppens, A. L. Falk, M. S. Rudner, H. Park, L. S. Levitov, C. M. Marcus, *Nano Lett.* **2011**, *11*, 4134.
[28] D. Basko, *Science* **2011**, *334*, 610.
[29] N. M. Gabor, J. C. W. Song, Q. Ma, N. L. Nair, T. Taychatanapat, K. Watanabe, T. Taniguchi, L. S. Levitov, P. J. Herrero, *Science* **2011**, *334*, 648.
[30] L. Britnell, R. V. Gorbachev, R. Jalil, B. D. Belle, F. Schedin, A. Mishchenko, T. Georgiou, M. I. Katsnelson, L. Eaves, S. V. Morozov, N. M. Peres, J. Leist, A. K. Geim, K. S. Novoselov, L. A. Ponomarenko, *Science* **2012**, *335*, 947.
[31] E. J. Lee, K. Balasubramanian, R. T. Weitz, M. Burghard, K. Kern, *Nat. Nanotechnol.* **2008**, *3*, 486.
[32] T. Takahashi, K. Takei, E. Adabi, Z. Y. Fan, A. M. Niknejad, A. Javey, *ACS Nano* **2010**, *4*, 5855.
[33] G. Chen, B. Liang, X. Liu, Z. Liu, G. Yu, X. M. Xie, T. Luo, D. Chen, M. Q. Zhu, G. Z. Shen, *ACS Nano* **2014**, *8*, 787.
[34] B. Liu, T. Luo, G. Mu, X. Wang, D. Chen, G. Shen, *ACS Nano* **2013**, *7*, 8051.
[35] X. Wang, W. Song, B. Liu, G. Chen, D. Chen, C. Zhou, G. Shen, *Adv. Funct. Mater.* **2013**, *23*, 1202.
[36] L. Zhu, X. Shen, Z. Zeng, H. Wang, H. Zhang, H. Chen, *ACS Nano* **2012**, *6*, 6033.
[37] X. Xu, Y. Zhao, E. J. Sie, Y. Lu, B. Liu, S. A. Ekahana, X. Ju, Q. Jiang, J. Wang, H. Sun, T. C. Sum, C. H. A. Huan, Y. P. Feng, Q. Xiong, *ACS Nano* **2011**, *5*, 3660.
[38] D. Li, J. Zhang, Q. Xiong, *ACS Nano* **2012**, *6*, 5283.
[39] C. Hsu, D. Lien, S. Lu, C. Chen, C. Kang, Y. Chueh, W. Hsu, J. H. He, *ACS Nano* **2012**, *6*, 6687.
[40] C. Y. Chen, J. R. D. Retamal, D. H. Lien, M. W. Chen, I. W. Wu, Y. Ding, Y. L. Chueh, C. I. Wu, J. H. He, *ACS Nano* **2012**, *6*, 9366.
[41] S. H. Tsai, H. C. Chang, H. H. Wang, S. Y. Chen, C. A. Lin, S. A. Chen, Y. L. Chueh, J. H. He, *ACS Nano* **2011**, *5*, 9501.
[42] Y. N. Guo, T. Burgess, Q. Gao, H. H. Tan, C. Jagadish, J. Zou, *Nano Lett.* **2013**, *13*, 5085.
[43] B. Tian, P. Xie, T. J. Kempa, D. C. Bell, C. M. Lieber, *Nat. Nanotechnol.* **2009**, *4*, 824.
[44] A. Pospischil, M. Humer, M. M. Furchi, D. Bachmann, R. Guider, T. Fromherz, T. Mueller, *Nat. Photonics.* **2013**, *7*, 892.
[45] X. Gan, R. J. Shiue, Y. Gao, I. Meric, T. F. Heinz, K. Shepard, J. Hone, S. Assefa, D. Englund, *Nat. Photonics.* **2013**, *7*, 883.
[46] X. Wang, Z. Cheng, K. Xu, H. K. Tsang, J. B. Xu, *Nat. Photonics.* **2013**, *7*, 888.
[47] K. K. Ng, *Complete Guide to Semiconductor Devices*, McGraw-Hill, New York, USA **1995**.
[48] S. J. Han, D. Reddy, G. D. Carpenter, A. D. Franklin, K. A. Jenkins, *ACS Nano* **2012**, *6*, 5220.
[49] X. Wan, K. Chen, D. Liu, J. Chen, Q. Miao, J. Xu, *Chem. Mater.* **2012**, *24*, 3906.
[50] H. Xu, Z. Zhang, H. Xu, Z. Wang, S. Wang, L. M. Peng, *ACS Nano* **2011**, *5*, 5031.
[51] D. R. Lide, *CRC Handbook of Chemistry and Physics*, 90th ed., CRC Press, Boca Raton **2010**.
[52] N. Han, F. Wang, J. J. Hou, S. P. Yip, H. Lin, F. Xiu, M. Fang, Z. Yang, X. Shi, G. Dong, T. F. Hung, J. C. Ho, *Adv. Mater.* **2013**, *25*, 4445.
[53] S. Adachi, *Handbook on Physical Properties of Semiconductors*, Springer Science & Business Media, Volume *2*, USA **2004**.

Received: August 2, 2014
Revised: September 22, 2014
Published online: October 31, 2014